NANO · MICRO small
www.small-journal.com

Benchmarking Phases of Ruthenium Dichalcogenides for Electrocatalysis of Hydrogen Evolution: Theoretical and Experimental Insights

Zhen Zhang, Cheng Jiang, Ping Li, Keguang Yao, Zhiliang Zhao, Jiantao Fan,* Hui Li,* and Haijiang Wang*

The hydrogen evolution reaction (HER) is a significant cathode step in electrochemical devices, especially in water splitting, but developing efficient HER catalysts remains a great challenge. Herein, comprehensive density functional theory calculations are presented to explore the intrinsic HER behaviors of a series of ruthenium dichalcogenide crystals (RuX_2, X = S, Se, Te). In addition, a simple and easily scaled production strategy is proposed to synthesize RuX_2 nanoparticles uniformly deposited on carbon nanotubes. Consistent with theoretical predictions, the RuX_2 catalysts exhibit impressive HER catalytic behavior. In particular, marcasite-type $RuTe_2$ ($RuTe_2$-M) achieves Pt-like activity (35.7 mV at 10 mA cm^{-2}) in an acidic electrolyte, and pyrite-type $RuSe_2$ presents outstanding HER performance in an alkaline media (29.5 mV at 10 mA cm^{-2}), even superior to that of commercial Pt/C. More importantly, a $RuTe_2$-M-based proton exchange membrane (PEM) electrolyzer and a $RuSe_2$-based anion exchange membrane (AEM) electrolyzer are also carefully assembled, and their outstanding single-cell performance points to them being efficient cathode candidates for use in hydrogen production. This work makes a significant contribution to the exploration of a new class of transition metal dichalcogenides with remarkable activity toward water electrolysis.

1. Introduction

In response to increasing levels of greenhouse gas emissions and rising global energy demands, various advanced technologies for generating environmentally friendly power have been developed. However, the fluctuating and intermittent, nature of renewable sources such as solar, wind, and tidal energy means these cannot be effectively collected and utilized. Fortunately, power-to-gas projects have been strongly encouraged, aiming to convert such fluctuating energy into hydrogen gas via water electrolysis.[1–3] The hydrogen can easily be stored in pressurized tanks, serving as a raw material for the chemical industry or for the synthesis of various hydrocarbon fuels, but also being reconverted to electricity when needed via fuel cells.[4,5] Traditional water electrolysis devices usually operate using liquid electrolyte, which has several drawbacks, including electrolyte leakage, sensitivity to CO_2 (especially in alkaline conditions), and low stability. Comparatively speaking, recently developed proton exchange membrane (PEM) and anion exchange membrane (AEM) electrolyzer techniques have notable advantages, including a high-purity H_2 product, and a safe, simple compact system.[6–11] Within an electrolyzer, the cathode hydrogen evolution reaction (HER) is a very significant step for water splitting and requires efficient catalysis.[12–15] To date, Pt remains the best electrocatalyst for the HER in acidic media; however, its high cost and scarcity seriously limit its use. More critically, in alkaline media, Pt exhibits two to three orders of magnitude lower HER conversion efficiency than in acidic media.[16,17]

Pyrite-phase metal dichalcogenides MX_2 (M = Fe, Co, Ni; X = S, Se, Te)[18–22] have demonstrated a certain degree of ability to catalyze the HER. Theoretical calculation and experimental results have proved that in addition to their active metal sites, the material's abundant sulfide and selenium can also serve as active centers to enable fast proton/electron adsorption and help accelerate the overall kinetics.[23–25] However, their activity and durability are still far from satisfactory in comparison with Pt. Moreover, the HER performance of MX_2 catalysts in acidic electrolytes is generally inferior.

Z. Zhang, K. Yao
School of Materials Science and Engineering
Harbin Institute of Technology
Harbin, Heilongjiang 150001, China
Z. Zhang, C. Jiang, K. Yao, Dr. Z. Zhao, Dr. J. Fan, Prof. H. Li
Department of Materials Science and Engineering
Shenzhen Key Laboratory of Hydrogen Energy
Southern University of Science and Technology
Shenzhen, Guangdong 518055, China
E-mail: fanjt@sustech.edu.cn; hui.li@sustech.edu.cn
Dr. P. Li
State Key Laboratory for Mechanical Behavior of Materials
Center for Spintronics and Quantum Systems
School of Materials Science and Engineering
Xi'an Jiaotong University
Xi'an, Shanxi 710049, China
E-mail: pli@xjtu.edu.cn
Prof. H. Wang
Department of Mechanical and Energy Engineering
Southern University of Science and Technology
Shenzhen, Guangdong 518055, China
The ORCID identification number(s) for the author(s) of this article can be found under https://doi.org/10.1002/smll.202007333.

DOI: 10.1002/smll.202007333

Very recently, Ru-based electrocatalysts have been extensively explored because of their Pt-like hydrogen binding strength and their good corrosion resistance in both acidic and alkaline media.[26–32] Most importantly, Ru is the least expensive platinum-group element. Yet, much less attention has been focused on ruthenium dichalcogenides (RuX_2, X = S, Se, Te) for the HER. Although a few papers have mentioned the synthesis of ruthenium disulfide for the HER,[33,34] the reported catalysts showed large particles and poor distribution on supports, so they could not realize their actual electrocatalytic capability. Hence, further efforts are much needed. With respect to ruthenium diselenides, no research about their HER performance has yet been reported. Ruthenium disulfide and diselenide have only a pyrite-type structure; whereas ruthenium ditellurides have two structures—the marcasite-type and the pyrite-type, but studies of their catalytic activity toward the HER are relatively few, especially for pyrite-type $RuTe_2$. The majority of ruthenium and tellurium-based catalysts are generally synthesized using telluride nanorods or nanoribbons as templates or supports,[35–37] which not only makes the preparation process more complicated but also implants large amount of inactive elemental Te. To date, no relevant theoretical analysis of their HER catalytic properties has been conducted, making a comprehensive theoretical and experimental study focused on this new family of RuX_2 catalysts for hydrogen electrolysis highly desirable as well as challenging.

We therefore undertook a through theoretical investigation of the intrinsic HER catalytic behaviors of RuX_2, including pyrite-type RuS_2, $RuSe_2$, and $RuTe_2$, and marcasite-type $RuTe_2$ using density functional theory (DFT) calculations. This included a detailed analysis of the binding energies of H, H_2O, and OH^-, as well as H_2O dissociation on the RuX_2 surfaces. Based on this analysis, we proposed a simple general strategy for fabricating a series of RuX_2 catalysts anchored on carbon nanotubes (CNT). We then carried out HER evaluation with a three-electrode configuration and we found that the RuX_2 exhibited impressive performance. Of these, the marcasite-type $RuTe_2$ catalyst demonstrated Pt-like HER activity (35.7 mV at 10 mA cm^{-2}) in an acidic electrolyte, and the pyrite-type $RuSe_2$ displayed the best performance in an alkaline medium, with a small overpotential of 29.5 mV at 10 mA cm^{-2} superior to that of commercial Pt/C. We then use the marcasite-type $RuTe_2$ and the $RuSe_2$ as cathode catalysts to constructed PEM and AEM electrolyzers, respectively. The catalysts' notable single-cell performance showed their strong potential for use in actual electrochemical water splitting.

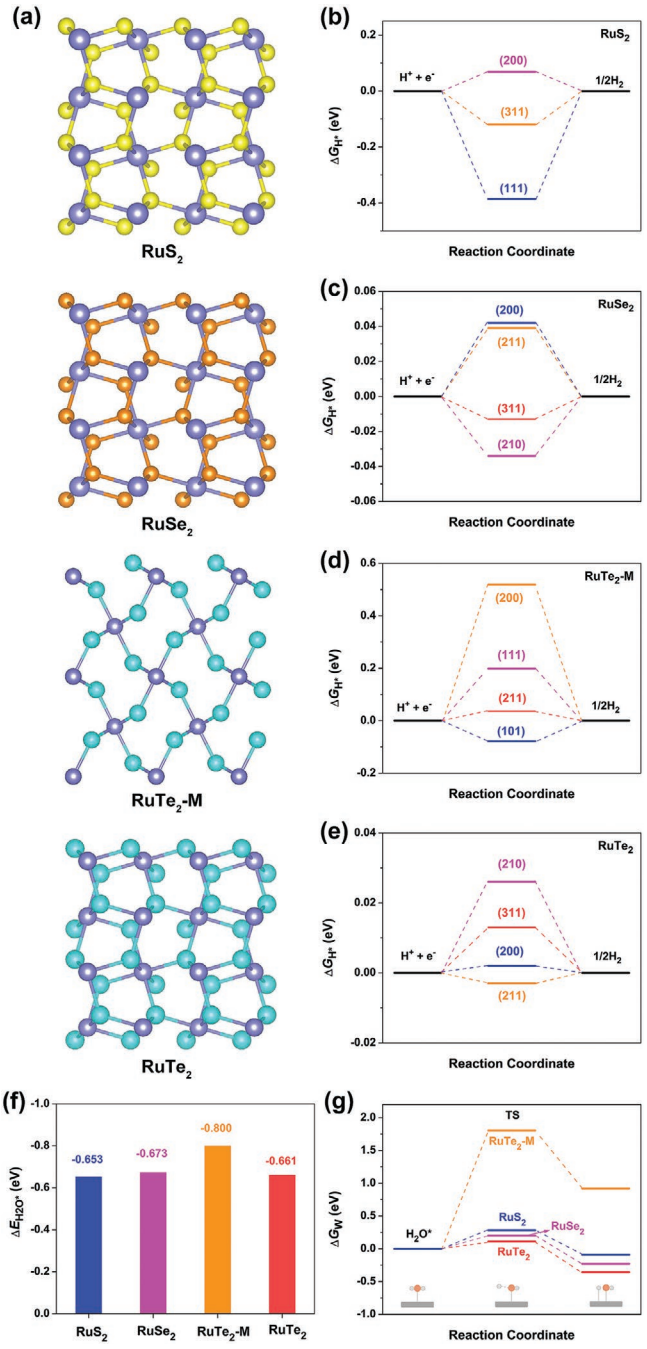

Figure 1. a) Crystal structures with exposed (002) planes. b–e) Free energy diagrams of H adsorption for RuS_2, $RuSe_2$, $RuTe_2$-M, and $RuTe_2$. f) H_2O binding energy and g) energy diagram of water dissociation for RuX_2.

2. Results and Discussion

2.1. Theoretical Calculation of RuX_2 Catalytic Activity toward the HER

Comprehensive DFT calculations were conducted to explore the intrinsic HER catalytic behavior of the ruthenium dichalcogenides. As shown in **Figure 1**a, RuS_2 and $RuSe_2$ exist as single-phase pyrite-type structures, while $RuTe_2$ has both pyrite-type and marcasite-type structures. These structural and compositional differences result in different electronic properties and catalytic features. For convenience, the pyrite-type RuS_2, $RuSe_2$, and $RuTe_2$ are denoted simply as RuS_2, $RuSe_2$, and $RuTe_2$, and the marcasite-type $RuTe_2$ is denoted as $RuTe_2$-M.

It is generally accepted that metal–hydrogen (M–H) binding energy is the sole descriptor for the hydrogen reaction in acidic media, and that Pt possesses optimal M–H strength, neither too weak nor too strong. Optimal HER activity can be achieved with a Gibbs free energy of hydrogen adsorption (ΔG_{H^*}) value close to zero.[38,39] The strongest main peaks in the standard

XRD patterns were selected as the crystal surfaces. We considered all of the initial adsorption sites for H atoms on the surfaces. The computed ΔG_{H^*} values are listed in Tables S1–S4, Supporting Information. The values of ΔG_{H^*} closest to 0 indicating the most favorable sites on the various planes are provide in Figure 1b–e. For RuS_2, the ΔG_{H^*} values of the (200) and (311) planes are 0.069 and -0.120 eV, very close to that of Pt (-0.09 eV),[40] implying a fast HER kinetic process. The (111) plane presents a comparable negative ΔG_{H^*} (-0.386 eV), suggesting stronger H binding ability; this creates the obstacle of thermodynamic H* desorption. The computed results for $RuSe_2$ confirmed that, the (111), (210), (211), and (311) planes deliver nearly zero ΔG_{H^*} values, making them efficient active sites for boosting the HER. The marcasite-type $RuTe_2$-M yields a negative ΔG_{H^*} (-0.078 eV) on the (101) surface, and slightly positive values on the (111) and (211), but still close to zero. However, the ΔG_{H^*} on (200) is 0.519 eV, meaning H is disinclined to be adsorbed in the initial step. Similarly, based on the computed ΔG_{H^*} values, the pyrite-type $RuTe_2$ provides moderate hydrogen binding on several planes.

For the computed H adsorption free energies of RuX_2, from RuS_2 to $RuTe_2$, the active sites show a possible switch from chalcogenide atoms to Ru atoms, which can be explained by the electron distribution and valence state. For chalcogenide atoms, the electronegativity is in the order of S > Se > Te, meaning that S may attract more electrons, thus enabling the higher oxidation state of Ru atoms. This phenomenon will be further elaborated by the later X-ray photoelectron spectroscopy (XPS) results. For the RuX_2 crystals, chalcogenide atoms can bring about difference on their catalytic performance. In addition to the above-mentioned electron distribution, the bonded dichalcogenide atoms can affect the electrical conductivities of RuX_2 crystals. Pyrite-type RuS_2 and $RuSe_2$ possess the bandgap of 0.68 and 0.48 eV, respectively, indicating a semiconductor character. However, $RuTe_2$ and $RuTe_2$-M exhibit the bandgap of 0.14 and 0.32 eV, implying Ru–Te are more metallic than RuS_2 and $RuSe_2$. Sufficient electrical conductivity could favor fast electron transport and promote catalytic process.

When the electrolyte is changed to an alkaline solution, the HER proceeds via the following Volmer–Tafel or Volmer–Heyrovsky mechanisms:[41]

$$\text{Volmer}: H_2O + e^- + * \leftrightarrow H_{ads} + OH^- \quad (1)$$

$$\text{Heyrovsky}: H_{ads} + H_2O + e^- \leftrightarrow H_2 + OH^- + * \quad (2)$$

$$\text{Tafel}: 2H_{ads} \leftrightarrow H_2 + 2* \quad (3)$$

In detail, the reaction pathway involves the adsorption of H_2O, the dissociation of H_2O into adsorbed OH^- and H atoms, the desorption of OH^- to leave a clean surface and the formation of H_2 from adsorbed H atoms.[42,43] Hence, in addition to M–H binding, M–H_2O/OH^- and water dissociation also matter.[44–46] Pt suffers from poor water dissociation ability, leading to dramatically decreased kinetics in alkaline media.[18] According to DFT calculations, the H_2O molecule binding energies ($\Delta E_{H_2O^*}$) of RuS_2, $RuSe_2$, $RuTe_2$-M, and $RuTe_2$ are -0.653, -0.673, -0.800, and -0.661 eV (Figure 1f). Such negative $\Delta E_{H_2O^*}$ values indicate that RuX_2 can easily capture H_2O, facilitating the fast Volmer process to generate protons. Water dissociation is a crucial subsequent step to break the OH–H bond and generate adsorbed OH* and H* species; the energy barrier for this is denoted as ΔG_w. As illustrated in Figure 1g, RuS_2, $RuSe_2$, and $RuTe_2$ exhibit very low ΔG_w values of 0.281, 0.199, and 0.111 eV smaller than that of Pt (0.66 eV).[47] However, the ΔG_w of $RuTe_2$-M is relatively large, suggesting inferior H_2O dissociation ability at the surface of the (200) plane. Low M–OH binding energy should also be preferable, as it allows the surface to be refreshed more easily. We therefore also constructed models of OH. As shown in Figure S1, Supporting Information, compared with the significantly ΔE_{OH^*} of Pt (–1.09 eV),[47] RuX_2 exhibit relatively weaker ΔE_{OH^*}. Their moderate H_2O/OH^- binding energies and low water dissociation energy barriers ensure fast kinetics during the Volmer step in an alkaline electrolyte. In summary, the above DFT calculations forecast that ruthenium dichalcogenides should possess superior intrinsic activity for the HER in both acidic and alkaline media.

2.2. Preparation and Characterization of RuX_2 Catalysts

A schematic diagram of the facile preparation of RuX_2 nanoparticles anchored on CNT support is depicted in **Figure 2**a. Commercial CNT support was first mildly oxidized through a modified Hummers method[48] to introduce oxygenated functional groups on their surface, which both enhanced their hydrophilia and encouraged the absorption of Ru^{3+} ions. The CNT/Ru^{3+} mixture was subsequently dried by lyophilization. Afterwards, the product was further annealed under an Ar atmosphere in a tube furnace, in which the S/Se/Te precursor was placed in the upstream section (Figure 2b). After the annealing treatment, RuX_2(X = S, Se, Te) nanoparticles were formed and uniformly deposited on the surface of the reduced oxidized-CNT.

The crystal structures of the RuX_2 were identified using powder X-ray diffraction (XRD). As illustrated in Figure 2c, all the catalysts exhibited two broad peaks at about 25.8° and 43°, which belong to the carbon diffractions of the CNT support. For RuS_2 annealed at 700 °C, several diffraction signals at 27.5°, 31.8°, 35.8°, 45.7°, and 54.1° can be assigned to the (111), (200), (210), (220), and (311) planes of cubic RuS_2 (JCPDS, no. 73-1677). When Se powder was used at 700 °C, the resulting catalyst shows characteristic peaks centered at 30.1°, 33.7°, 37.0°, 43.1°, and 51.0°, which correspond well to the (200), (210), (211), (220), and (311) planes, indicating the formation of cubic $RuSe_2$ (JCPDS, no. 80-0670).

As mentioned in the calculation section, $RuTe_2$ possesses both a pyrite-type cubic structure and a marcasite-type orthorhombic structure. In the XRD pattern of $RuTe_2$ annealed at 700 °C, the main peaks at 21.8°, 27.8°, 31.3°, 32.7°, 33.9°, and 43.3° index to the (110), (101), (111), (120), (200), and (211) facets of orthorhombic $RuTe_2$ (JCPDS, no. 88-1380). To synthesize cubic $RuTe_2$, a series of annealing treatments under various temperatures was carried out. The XRD patterns of the resulting catalysts are shown in Figure S2, Supporting Information. When the temperature was increased to 850 °C, the diffraction signals related to marcasite-type $RuTe_2$ nearly

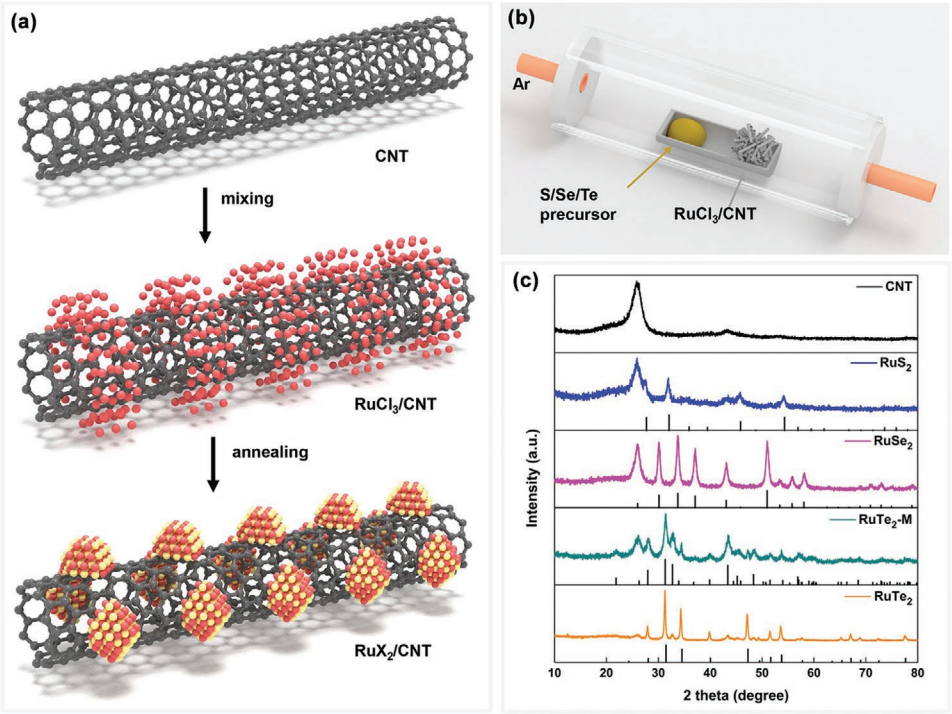

Figure 2. Synthesis and structure of RuX_2 catalysts. a,b) Schematic illustrations of the synthesis procedure and annealing treatment. c) XRD patterns of RuS_2, $RuSe_2$, and $RuTe_2$-M obtained annealed at 700 °C, and of $RuTe_2$ annealed at 850 °C.

disappeared, leaving the peaks consistent with cubic $RuTe_2$ (JCPDS, no. 19-1108), which suggested the major product at this temperature was pyrite-type $RuTe_2$. As the temperature was further increased, the cubic $RuTe_2$ was gradually reduced to become hcp Ru metal (JCPDS, no. 06-0663). In summary, pure pyrite-type RuX_2 and marcasite-type $RuTe_2$ were synthesized by regulating the annealing conditions. This is the first time a facile method for systematically designing and synthesizing the whole crystal structures of ruthenium dichalcogenides has been reported.

The morphologies of RuX_2 were characterized by scanning electron microscopy (SEM) and transmission electron microscopy (TEM). The SEM images (Figure S3, Supporting Information) exhibit the characteristic features of CNT structures, with smooth, clean surfaces. Energy-dispersive X-ray spectroscopy (EDS) (Figure S4, Supporting Information) verified that the atomic ratios of Ru to X were just slightly larger than but greatly approximate to 1:2. The slight additional X component will be discussed later in relation to our XPS analysis. Notably, the low-resolution TEM image (**Figure 3**a) shows RuS_2 nanoparticles uniformly dispersed on the surface of the CNT support. The size of the major nanoparticles was concentrated in the narrow range of 2–5 nm, with an average size of 3.3 nm. Small particle size and homogeneous distribution may have favored the exposure of sufficient active sites, while the CNT would have enabled fast electron transport, thereby synergistically accelerating the catalytic process. The high-resolution TEM (HRTEM) (Figure 3b) image clearly reveals multiple layers with a space of 0.34 nm, corresponding to the (002) plane of carbon, suggesting the CNT's high degree of graphitization. Lattice fringes with spacings of 0.25 and 0.28 nm are also observable, associated with the (210) and (200) crystal planes of cubic RuS_2. The TEM image (Figure 3c) for $RuSe_2$ shows a broader size range (3–12 nm) as well as a larger average size of 6.7 nm. Apart from the (002) planes of carbon, lattice fringes with spaces of 0.26, 0.29, and 0.34 nm were present, as shown in Figure 3d, consistent with the distances of the (210), (200), and (111) planes of pyrite-type $RuSe_2$.

In comparison, after Ru was alloyed with Te at 700 °C, the resulting $RuTe_2$-M catalyst (Figure 3e) demonstrated less homogeneity of particle size, and the average size increased to approximately 7.1 nm. As can be clearly seen in Figure 3f, marcasite-type $RuTe_2$-M particles were closely anchored on the CNT surfaces, and the (101), (111), and (200) facets of $RuTe_2$-M could be identified. When the temperature was increased to 850 °C, the as-prepared $RuTe_2$ displayed larger aggregate particles with an average size of about 12.8 nm (Figure 3g). The lattice fringes with a spacing of 0.26 nm displayed in Figure 3h are consistent with the (211) crystal planes of cubic $RuTe_2$.

To further explore the chemical composition and electronic configuration of RuX_2, we carried out XPS measurements. The high-resolution Ru 3p spectra of the RuX_2 catalysts shown in **Figure 4**a indicate the existence of two obvious Ru $3p_{1/2}$ and Ru $3p_{3/2}$ regions, which can be fitted to two doublets. The peaks of Ru $3p_{1/2}$ for RuS_2 and $RuSe_2$ exhibit positive shifts (0.9 and 0.5 eV, respectively) to higher binding energy compared to that of $RuTe_2$, strongly confirming the electron transfer from Ru to S. In the high-resolution S 2p spectrum of RuS_2 (Figure 4b), two main peaks located at 163.8 eV (S $2p_{1/2}$) and 162.6 eV (S $2p_{3/2}$) can be observed, assignable to the Ru—S bond. A S—C signal was also detected, implying the doping of S into the CNT; this is why the EDS results showed the number of S

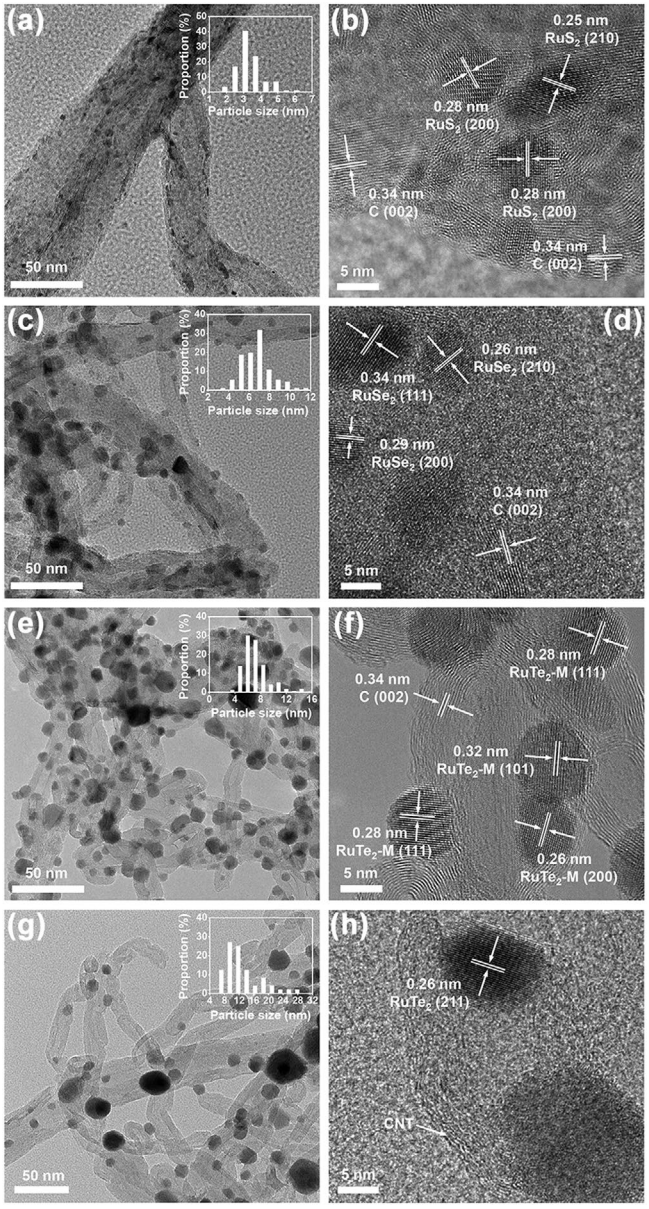

Figure 3. TEM images for a,b) RuS_2, c,d) $RuSe_2$, e,f) $RuTe_2$-M, and g,h) $RuTe_2$. Insets in (a, c, e, g) are the corresponding particle size distributions.

atoms to be slightly larger than twice the amount of Ru. The existence of a S—O signal was due to unavoidable surface oxidation.[49] Figure 4c presents the Se 3d spectrum, in which two peak regions at 55.8 and 55.0 eV correspond to Se $3d_{3/2}$ and Se $3d_{5/2}$, respectively, in the Ru—Se bond.[50] Peaks at 59.1 and 58.3 eV arose from SeO_2 caused by surface oxidation under ambient conditions.[51] Apart from the above Se species, a small amount of Se was observed, possibly due to excess deposition during annealing. The high-resolution Te 3d spectra for $RuTe_2$-M and $RuTe_2$ (Figure 4d,e) show four peaks: a pair at 584.1 and 573.7 eV, corresponding to the Ru—Te bond, and another pair at 586.7 and 576.3 eV, indexed to the TeO_2 oxidation state.[52]

The nitrogen (N_2) adsorption-desorption isotherms of the RuX_2 as-prepared catalysts were also obtained to investigate the Brunauer-Emmett-Teller (BET) specific surface areas (Figure S5, Supporting Information), which were calculated to be 118.5, 173.1, 123.8, and 134.8 $m^2\ g^{-1}$ for RuS_2, $RuSe_2$, $RuTe_2$-M, and $RuTe_2$. All of the BET results are listed in Table S5, Supporting Information. Overall, the CNT support played crucial roles: 1) the oxygenated functional groups on their surface favored the anchoring of Ru species and enabled the uniform distribution of RuX_2 particles during annealing; 2) CNT support with a high degree of graphitization provided fast electron transport pathways; 3) the CNT's high surface area and sufficient pores facilitated contact with the electrolyte and the release of hydrogen gas.

2.3. HER Investigation of RuX_2 Catalysts Using Three-Electrode Configuration

The electrochemical HER performance of the RuX_2 catalysts was investigated in Ar-saturated acidic 0.5 M H_2SO_4 and alkaline 1.0 M KOH using a three-electrode configuration. For comparison, commercial Pt/C catalyst was also evaluated under the same conditions. **Figure 5**a shows the LSV curves (*iR* compensated) of RuX_2 and Pt/C in 0.5 M H_2SO_4. The RuX_2 catalysts clearly exhibited distinct HER behavior. To drive a current density of 10 mA cm^{-2}, RuS_2, $RuSe_2$, $RuTe_2$-M, and $RuTe_2$ required overpotentials of only 54.5, 87.8, 35.7, and 51.7 mV. Notably, $RuTe_2$-M showed the best HER activity, with only a small overpotential of 92.3 mV at a high current density of 100 mA cm^{-2}, very close to that of Pt/C. Figure 5b presents the Tafel plots of the corresponding polarization curves. Commercial Pt/C delivered the lowest Tafel slope of 33.7 mV dec^{-1}, suggesting the Volmer–Tafel mechanism as the HER pathway. For the RuX_2 catalysts, the resulting Tafel slopes were 65.3, 70.3, 46.6, and 56.4 mV dec^{-1} for RuS_2, $RuSe_2$, $RuTe_2$-M, and $RuTe_2$, indicating the Volmer–Heyrovsky mechanism for HER. The exchange current densities were derived by extrapolation of the Tafel plots and are shown in Figure 5c. $RuTe_2$-M delivered a high exchange current density of 1.71 mA cm^{-2}. We also conducted electrochemical impedance spectroscopy (EIS) measurements with an overpotential of –25 mV. The Nyquist plots (Figure S6, Supporting Information) confirmed that $RuTe_2$-M exhibited the lowest charge transfer resistance among the RuX_2 catalysts, which was consistent with the trend in their HER activities. The durability of the materials' HER catalytic performance in the acidic electrolyte was investigated by conducting continuous cyclic voltammetry (CV) at a scan rate of 50 mV s^{-1}. The LSV plots of RuX_2 after 2000 cycles (Figure S7, Supporting Information) showed only very slight degradation. In addition, the time-dependent current density curves for $RuTe_2$-M indicated only negligible attenuation after 15 h (Figure S8, Supporting Information), implying its outstanding stability.

XRD patterns for RuX_2 after stability testing in acidic electrolyte are provided in Figure S9 in the Supporting Information. We found that RuS_2, $RuSe_2$, $RuTe_2$ catalysts maintained their pyrite-type structure, and $RuTe_2$-M still displayed its marcasite-type crystallinity. XPS measurements (Figure S10, Supporting Information) after HER test are also presented. No apparent variation was found for the binding energy of Ru element, suggesting good stability. For Te element of $RuTe_2$-M and $RuTe_2$,

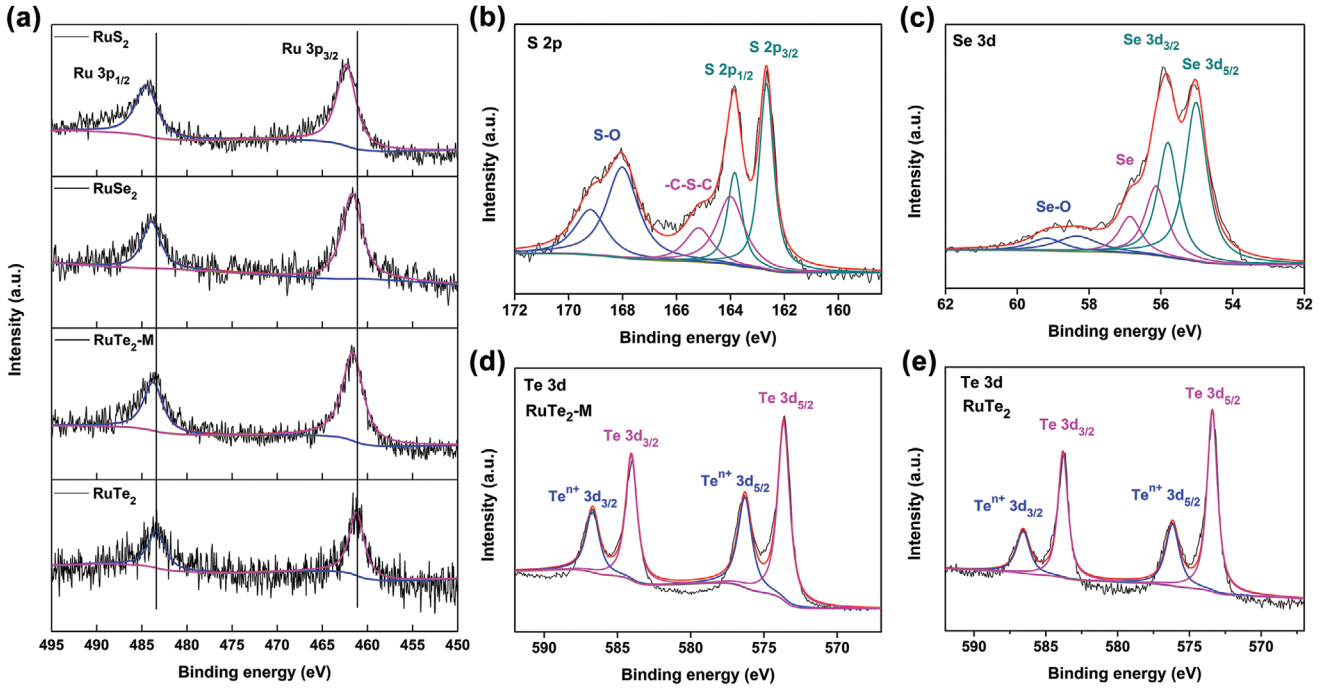

Figure 4. XPS spectra of a) Ru 3p, b) S 2p of RuS_2, c) Se 3d of $RuSe_2$, d) Te 3d of $RuTe_2$-M, and e) Te 3d of $RuTe_2$.

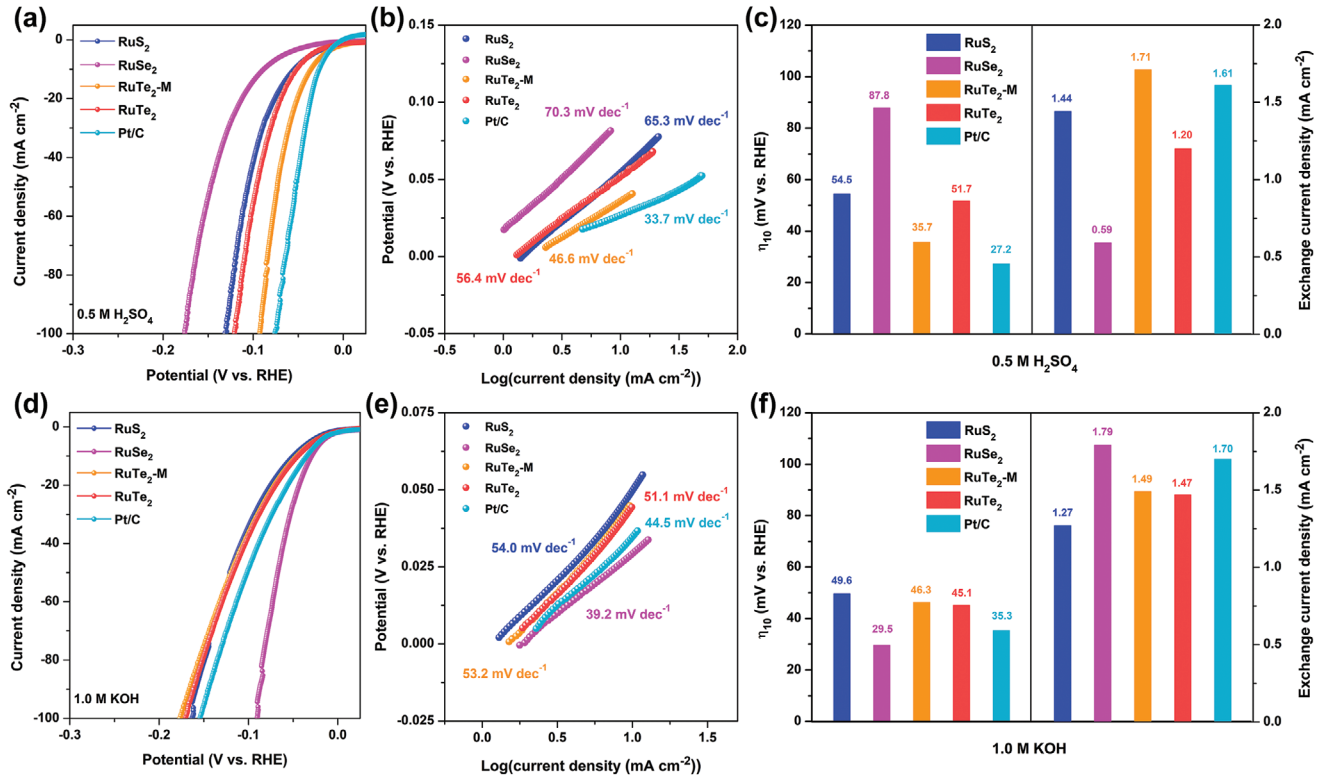

Figure 5. Electrochemical HER performance using a three-electrode system: a) polarization curves, b) corresponding Tafel plots, c) overpotential at 10 mA cm^{-2} and exchange current density of RuX_2 and Pt/C catalysts in Ar-saturated 0.5 M H_2SO_4 solution. d) Polarization curves, e) corresponding Tafel plots, f) overpotential at 10 mA cm^{-2} and exchange current density of RuX_2 and Pt/C catalysts in Ar-saturated 1.0 M KOH.

there was no obvious change on the binding energy, while the content of oxidized Te was clearly decreased, which was due to the partial reduction of surface oxidation for Ru–Te under HER reduction conditions.

In the DFT calculation prediction, $RuTe_2$ exhibits moderate hydrogen binding and seems to have a better activity for HER; however, experimentally, $RuTe_2$-M catalyst showed the best HER activity in acidic condition. In this work, in order to predicate the HER activity and simplify the computations, we constructed the models only based on the pure pyrite-type and marcasite-type RuX_2 crystals. However, during the actual catalyst preparation, the CNT support, the interface effect between CNT and RuX_2, and even the excessive chalcogenide atoms or their oxides can be more complicated and may lead to a certain degree of influence on HER performance. For example, the doping of X atoms into the CNT may occur during high-temperature annealing treatment, especially for RuS_2. The ΔG_{H^*} of pure CNT support is too positive and cannot efficiently absorb H*. The X dopants into CNT can introduce structure defects, which are related to the active sites[53,54] and meanwhile generate an interface effect between CNT and RuX_2 nanoparticles. In addition, X atoms are easily and inevitably oxidized while being exposed with air, leading to the formation of S-O_x, Se-O_x and Te-O_x, which have been identified by the XPS results. According to the Te 3d spectra in Figure 4d,e, the intensity of Te—O bond peaks for $RuTe_2$-M is relatively higher than that of $RuTe_2$. Hence, we speculate that the surface oxidation of Te species may also cause an influence on the H* absorption. Moreover, $RuTe_2$ showed relatively poor HER stability, and the Te 3d spectra indicated that the surface oxidized Te species were evidently reduced, again proving the suitable surface oxidation is another factor responsible for the HER activity.

We also measured the RuX_2 catalysts' activity toward the HER in an alkaline environment. The potential was calibrated with respect to a reverse hydrogen electrode (RHE; details of the RHE calibration can be found in the experimental section and Figure S11, Supporting Information) and corrected with *iR* compensation (Figure 5d). Compared with the results in the acidic solution, commercial Pt/C provided inferior HER activity, requiring overpotentials of 35.3 and 154.7 mV to drive current densities of 10 and 100 mA cm^{-2}. Notably, the RuX_2 catalysts performed well in the alkaline electrolyte. Specifically, at a current density of 10 mA cm^{-2}, RuS_2, $RuSe_2$, $RuTe_2$-M, and $RuTe_2$ displayed overpotentials of 49.6, 29.5, 46.3, and 45.1 mV. Importantly, $RuSe_2$ presented the highest HER activity, requiring only 90.1 mV at a high current density of 100 mA cm^{-2}, much lower than Pt/C. After fitting (Figure 5e), Tafel slopes of 54.0, 39.2, 53.2, and 51.1 mV dec^{-1} were obtained for RuS_2, $RuSe_2$, $RuTe_2$-M, and $RuTe_2$. The value of the Tafel slope for $RuSe_2$ was between 30 and 40 mV dec^{-1}, implying that its HER behavior in an alkaline medium followed the efficient Volmer–Tafel mechanism. Notably, the exchange current density of $RuSe_2$ (1.79 mA cm^{-2}) was higher than that of Pt/C (1.70 mA cm^{-2}) (Figure 5f). EIS measurements were also carried out in the alkaline electrolyte using an overpotential of −25 mV, and the results are provided in Figure S12, Supporting Information. As expected, $RuSe_2$ exhibited the smallest charge transfer resistance, again confirming its outstanding HER activity. The RuX_2 catalysts' remarkable HER performance in alkaline media—comparable and in some cases superior to that of Pt/C—was consistent with the theoretical predictions and largely attributable to the synergistic effect associated with favorable H binding energies and low water dissociation energy barriers. We tested the stability of their HER performance using continuous CV. After 2000 CV cycles, RuS_2 and $RuSe_2$ demonstrated better stability than $RuTe_2$-M and $RuTe_2$ (Figure S13, Supporting Information). In addition, after lengthy *i–t* testing (Figure S14, Supporting Information), the current density of $RuSe_2$ was undiminished, confirming its good electrochemical HER stability. After HER test, the crystal structures of RuX_2 remain unchanged according to the XRD patterns (Figure S15, Supporting Information). For the elemental valence states (Figure S16, Supporting Information), the decrease of Te–O content was also observed, which is due to the reduction of partial surface oxidation. Notably, the HER performance values of RuX_2 catalysts compare favorably with those of most previously studied Ru-based HER catalysts in both acidic and alkaline media (Tables S6 and S7, Supporting Information).

2.4. PEM- and AEM-Based Electrolyzer Measurements

To further demonstrate that these catalysts have advanced practical use for hydrogen production, PEM and AEM-based electrolyzer devices with oxygen and hydrogen evolution electrodes were carefully assembled. $RuTe_2$-M and $RuSe_2$ were chosen as the HER catalysts for the PEM and AEM electrolyzers, respectively. For the anode catalyst, commercial IrO_2 was used to catalyze the oxygen evolution reaction (OER). Photographs of a homemade electrolyzer and prepared catalyst-coated membranes (CCMs) are displayed in Figures S17 and S18, Supporting Information.

Figure 6a is a schematic diagram of the components in the PEM electrolyzer. A cross-sectional SEM image of the corresponding CCM (IrO_2//$RuTe_2$-M) is shown in Figure S19a, Supporting Information. During operation, deionized water was consistently pumped into the anode side, where it was split via the OER to produce sufficient protons. The resulting protons moved from anode to cathode through the PEM and were reduced to H_2 gas at the cathode. At 80 °C, the cell delivered current densities of 0.68 and 0.25 A cm^{-2} at voltages of 1.8 and 1.6 V (Figure 6b). The performance clearly improved as the operation temperature increased from room temperature to 80 °C. Figure S20a, Supporting Information, presents the Nyquist plots measured at different temperatures with a voltage of 1.6 V. The charge transfer resistance decreased with increasing temperature, which accords with the results of the polarization curves.

Figure 6c shows the components of the AEM electrolyzer and Figure S19b, Supporting Information, presents a cross-sectional SEM image of the actual corresponding CCM (IrO_2// $RuSe_2$). Unlike with the PEM electrolyzer, an alkaline solution needed to be consistently injected into the cathode side. After the cathode HER electrocatalysis process, water was decomposed into H_2 gas and free anions, and the voltage then drove these anions through the AEM to the anode side to supply the OER. At room temperature, the AEM electrolyzer exhibited a current density of 0.73 A cm^{-2} at a voltage of 1.8 V. The

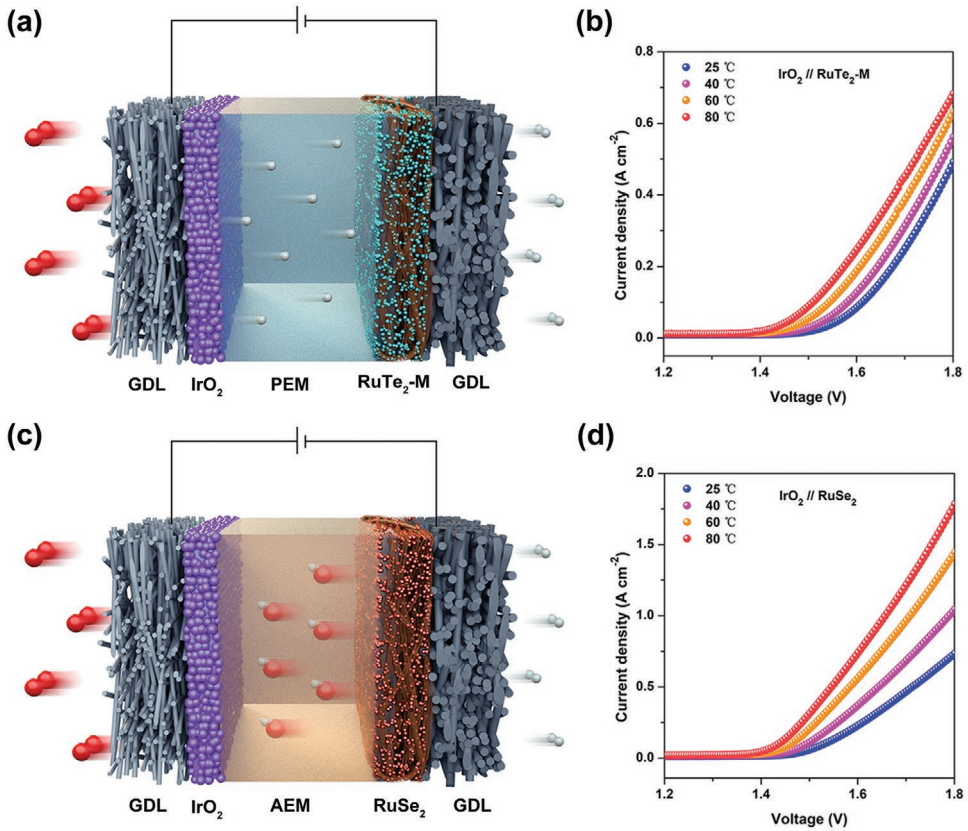

Figure 6. a) Schematic diagram of single-cell components and b) polarization curves operated at different cell temperatures in a PEM electrolyzer (IrO_2//$RuTe_2$-M). c) Schematic diagram of single-cell components and d) polarization curves operated at different cell temperatures in an AEM electrolyzer (IrO_2//$RuSe_2$).

performance increased as the temperature rose (Figure 6d). Surprisingly, high current densities of 1.78 and 0.74 A cm^{-2} were obtained with voltages of 1.8 and 1.6 V at 80 °C. In addition, Nyquist plots (Figure S20b, Supporting Information) revealed decreased charge transfer resistance at higher temperatures. These primary HER evaluations with the three-electrode configuration and the electrolyzer measurements confirmed the RuX_2 catalysts' potential for practical use in electrochemical water splitting. For comparison, we also assembled PEM and AEM electrolyzers using commercial Pt/C as the cathode catalyst with a final Pt loading of 0.1 mg cm^{-2}. Pt/C showed outstanding electrocatalytic HER performance in the acidic medium, better than that of $RuTe_2$-M (Figure S21a, Supporting Information). However, in the alkaline AEM electrolyzer, Pt/C delivered inferior performance (Figure S21b, Supporting Information). At 80 °C, the current density of the $RuSe_2$ AEM electrolyzer at 1.8 V was almost 4.5 times that of commercial Pt/C.

3. Conclusion

In this work, we first carried out detailed theoretical calculations for ruthenium dichalcogenides (RuX_2, X = S, Se, Te), including their hydrogen binding energies and water dissociation abilities at various lattice planes, the results of which verified their strong HER activity in both acidic and alkaline media. We also successfully fabricated RuX_2 nanoparticles of various crystal types (pyrite-type RuS_2, $RuSe_2$, and $RuTe_2$, and marcasite-type $RuTe_2$) using a simple and easily scalable synthesis process. Three-electrode system testing demonstrated that the RuX_2 catalysts exhibited notable HER catalytic behavior in both acidic and alkaline media. Finally, we achieved excellent performance with a $RuTe_2$-M-based PEM electrolyzer and a $RuSe_2$-based AEM electrolyzer, further highlighting the materials' strong potential for actual hydrogen production. This work provides a roadmap for developing a new generation of transition metal-based dichalcogenide catalysts with superior performance toward electrochemical water splitting.

4. Experimental Section

Synthesis of RuX_2 (RuS_2, $RuSe_2$, $RuTe_2$-M, and $RuTe_2$) /CNT: The multiwalled CNTs were oxidized by a modified Hummers method. The oxidized CNTs (100 mg) were dispersed in water (50 mL) by sonication for 20 min and magnetic stirring for 30 min. Then $RuCl_3{\cdot}xH_2O$ aqueous solution (5 mg mL^{-1}, 6 mL) was injected slowly under stirring. This mixture was further magnetically stirred for 6 h at room temperature. After that, the resulting precursor was dried by lyophilization. The obtained mixture was put into a porcelain boat, which was then placed at the center of a quartz tube in a horizontal tube furnace. L-cysteine/Se powder/Te powder were used as the S/Se/Te precursors, respectively, and each was placed in the upstream region of the furnace. Afterward, the samples were annealed at 700 °C for 1 h under an Ar atmosphere,

then allowed to cool naturally to room temperature. For the Ru–Te/CNT samples, the precursors were also annealed at 800, 850, 900, and 1000 °C. The samples of RuS_2 (700 °C), $RuSe_2$ (700 °C), and $RuTe_2$ (850 °C) possessed a pyrite-phase structure; these are denoted simply as RuS_2, $RuSe_2$, and $RuTe_2$. The $RuTe_2$ product annealed at 700 °C exhibited a marcasite structure, which is denoted as $RuTe_2$-M.

Materials Characterizations: The catalysts' morphologies were characterized by a TESCAN field emission scanning electron microscope (SEM). Transmission electron microscopy (TEM) and high-resolution transmission electron microscopy (HRTEM) were conducted using a JEOL-2100F instrument. Powder X-ray diffraction (XRD) for structural identification was performed on a Bruker AXS D8-Focus with Cu Kα radiation (γ = 1.54056 Å). X-ray photoelectron spectroscopy (XPS) measurements were carried out with a PHI 5000 Versa Probe III. The specific surface area and pore size distributions were obtained from nitrogen adsorption-desorption isotherms collected at 77 K on a Micromeritics ASAP 2020 physisorption instrument using the Brunauer-Emmett-Teller (BET) and Barrett-Joyner-Halenda (BJH) methods.

Three-Electrode Electrochemical Measurements: Electrochemical measurements were carried out with a Solartron electrochemical workstation under ambient temperature using a typical three-electrode configuration, in which a glassy carbon rotating disk electrode (RDE) with a diameter of 5 mm (a disk geometric area of 0.196 cm^2), and a graphite rode were applied as the working electrode, and counter electrode, respectively. A reversible hydrogen electrode (RHE) and a Hg/HgO electrode were used as the reference electrode in acidic and alkaline media, respectively. The potential of Hg/HgO detected was calibrated with respect to RHE. Specially, a Pt foil was used as the working electrode, and high-purity hydrogen gas was continuously pumped into the electrolyte. Cyclic voltammetry (CV) testing was performed at a scan rate of 1 mV s^{-1}, and the average value of the two potentials corresponding to zero current was taken as the thermodynamic potential for the hydrogen electrode reactions. For the catalyst ink preparation, each catalyst (5 mg) and 50 µL of Nafion solution (5 wt%) were dispersed in 1 mL of water/ethanol (v:v, 1:3) solution. After sonication for 30 min in an ice bath, the catalyst ink (18 µL) was then dropped onto the surface of the RDE. For the HER measurements, linear sweep voltammetry (LSV) was recorded at a scan rate of 5 mV s^{-1} at room temperature. Ar-saturated 0.5 M H_2SO_4 and 1.0 M KOH were used as the acidic and alkaline electrolytes, respectively. Electrochemical impedance spectroscopy (EIS) was conducted in a frequency range of 10 0000–0.1 Hz. The polarization curves were all corrected with *iR*-compensation according to the EIS results. The Tafel slopes were fitted based on the Tafel equation ($\eta = a + b\log(j)$), where η (mV) indicates the applied overpotential, j (mA cm^{-2}) denotes the current density, and b (mV dec^{-1}) is the Tafel slope.

Single-Cell Electrochemical Measurements: For the PEM water electrolyzer, IrO_2 was used as the anode catalyst for the oxygen evolution reaction (OER) and $RuTe_2$-M was used as the cathode HER catalyst. For the anode, 50 mg of IrO_2 powder was homogeneously dispersed in 5 mL of water/isopropyl alcohol (IPA) (v:v, 1:9) solution with the addition of 125 mg of Nafion (10 wt%) solution under sonication for 1h. For the cathode, 10 mg of $RuTe_2$-M was added into to 2 mL of water/IPA solution with the addition of 45 mg of Nafion solution. Afterwards, a PEM (Gore M820.15) was fixed onto a heating plate. The catalyst inks were directly air-sprayed on both sides of the PEM, with an IrO_2 loading of 2.5 mg cm^{-2} for anode and a $RuTe_2$-M loading of 2 mg cm^{-2} for the cathode. The resulting catalyst-coated membrane (CCM) was then hot-pressed at 160 °C with 60 psi for 30 s.

For the AEM water electrolyzer, FAA-3-50 (Fumatech, Germany) was used as the AEM. The AEM was pretreated in 1.0 M KOH solution at 80 °C for 1 h, and then washed with water three times. The catalyst slurry preparation was similar to that of the PEM-based CMM, except FAA-3-Br was used as the anion polymer, and $RuSe_2$ was used as the cathode catalyst. For comparison, commercial Pt/C (10 wt%) was also used as the cathode catalyst for PEM and AEM electrolyzers. The final Pt loading was fixed at 0.1 mg cm^{-2}.

The resulting CCMs were then pressed between the anode and cathode gas diffusion layers (GDLs) to form the membrane electrode assembly (MEA). Finally, the MEAs were fixed by flow field plates, fluorinated ethylene propylene gaskets, and end plates using a torque of 5 N. During electrolyzer testing, water and 1.0 M KOH solution were preheated and then continuously pumped through the PEM and AEM electrolyzers, respectively. The electrolyzers were evaluated by stepping the voltage from 1.0 to 1.8 V. In addition, EIS measurements were carried out over a frequency range from 100 kHz to 10 Hz with an initial voltage of 1.6 V.

DFT Calculations: All the calculations on the atomic structure and binding energies of the chosen system were carried out using spin-polarized density functional theory (DFT) with generalized gradient approximation (GGA) for exchange-correlation potential embedded in Vienna Ab Initio Simulation Package (VASP). The energy cut off for the plane-wave expansion was established as 400 eV. All structures were allowed to relax during structure optimization, and the maximum force on the atoms was set at 0.05 eV $Å^{-1}$.

Supporting Information

Supporting Information is available from the Wiley Online Library or from the author.

Acknowledgements

This work was financially supported by the National Key Research and Development Program of China (2017YFB0102701), the Shenzhen Peacock Plan (KQTD2016022620054656), the Development and Reform Commission of Shenzhen Municipality 2017 (No. 1106), the Guangdong Innovative and Entrepreneurial Research Team Program (2016ZT06N500), the Postdoctoral Science Foundation funded project (No. 2020M673364), the Natural Science Foundation for Distinguished Young Scholars of Hunan Province (No. 2018JJ1022), and the National Natural Science Foundation of China Grant (Nos. 12004295).

Conflict of Interest

The authors declare no conflict of interest.

Data Availability Statement

The data that support the findings of this study are available from the corresponding author upon reasonable request.

Keywords

AEM electrolyzer, hydrogen evolution reaction, PEM electrolyzer, ruthenium dichalcogenides

Received: November 23, 2020
Revised: January 7, 2021
Published online: February 15, 2021

[1] A. Saeedmanesh, M. A. Mac Kinnon, J. Brouwer, *Curr. Opin. Electrochem.* **2018**, *12*, 166.
[2] S. Schiebahn, T. Grube, M. Robinius, V. Tietze, B. Kumar, D. Stolten, *Int. J. Hydrogen Energy* **2015**, *40*, 4285.
[3] X. Shi, Y. Qian, S. Yang, *ACS Sustainable Chem. Eng.* **2020**, *8*, 7097.

[4] D. Parra, L. Valverde, F. J. Pino, M. K. Patel, *Renewable Sustainable Energy Rev.* **2019**, *101*, 279.
[5] M. D. Bhatt, J. Y. Lee, *Energy Fuels* **2020**, *34*, 6634.
[6] Q. Feng, X. Z. Yuan, G. Liu, B. Wei, Z. Zhang, H. Li, H. Wang, *J. Power Sources* **2017**, *366*, 33.
[7] H. A. Miller, K. Bouzek, J. Hnat, S. Loos, C. I. Bernäcker, T. Weißgärber, L. Röntzsch, J. Meier-Haack, *Sustainable Energy Fuels* **2020**, *4*, 2114.
[8] Y. S. Park, J. Yang, J. Lee, M. J. Jang, J. Jeong, W.-S. Choi, Y. Kim, Y. Yin, M. H. Seo, Z. Chen, S. M. Choi, *Appl. Catal., B* **2020**, *278*, 119276.
[9] N. Yousfi-Steiner, P. Moçotéguy, D. Candusso, D. Hissel, *J. Power Sources* **2009**, *194*, 130.
[10] P. K. R. Holzapfel, M. Bühler, D. Escalera-López, M. Bierling, F. D. Speck, K. J. J. Mayrhofer, S. Cherevko, C. V. Pham, S. Thiele, *Small* **2020**, *16*, 2003161.
[11] Z. L. Zhao, Q. Wang, X. Huang, Q. Feng, S. Gu, Z. Zhang, H. Xu, L. Zeng, M. Gu, H. Li, *Energy Environ. Sci.* **2020**, *13*, 5143.
[12] Z. Chen, X. Duan, W. Wei, S. Wang, B.-J. Ni, *Nano Energy* **2020**, *78*, 105270.
[13] F. Yu, L. Yu, I. K. Mishra, Y. Yu, Z. F. Ren, H. Q. Zhou, *Mater. Today Phys.* **2018**, *7*, 121.
[14] L. Lin, P. Sherrell, Y. Liu, W. Lei, S. Zhang, H. Zhang, G. G. Wallace, J. Chen, *Adv. Energy Mater.* **2020**, *10*, 1903870.
[15] A.-Y. Lu, X. Yang, C.-C. Tseng, S. Min, S.-H. Lin, C.-L. Hsu, H. Li, H. Idriss, J.-L. Kuo, K.-W. Huang, L.-J. Li, *Small* **2016**, *12*, 5530.
[16] J. Mohammed-Ibrahim, X. Sun, *J. Energy Chem.* **2019**, *34*, 111.
[17] N. Mahmood, Y. Yao, J.-W. Zhang, L. Pan, X. Zhang, J.-J. Zou, *Adv. Sci.* **2018**, *5*, 1700464.
[18] T. Wang, H. Xie, M. Chen, A. D'Aloia, J. Cho, G. Wu, Q. Li, *Nano Energy* **2017**, *42*, 69.
[19] D. Kong, J. J. Cha, H. Wang, H. R. Lee, Y. Cui, *Energy Environ. Sci.* **2013**, *6*, 3553.
[20] I. H. Kwak, H. S. Im, D. M. Jang, Y. W. Kim, K. Park, Y. R. Lim, E. H. Cha, J. Park, *ACS Appl. Mater. Interfaces* **2016**, *8*, 5327.
[21] T.-H. Lu, C.-J. Chen, M. Basu, C.-G. Ma, R.-S. Liu, *Chem. Commun.* **2015**, *51*, 17012.
[22] B. Dutta, Y. Wu, J. Chen, J. Wang, J. He, M. Sharafeldin, P. Kerns, L. Jin, A. M. Dongare, J. Rusling, S. L. Suib, *ACS Catal.* **2019**, *9*, 456.
[23] F. Wang, Y. Li, T. A. Shifa, K. Liu, F. Wang, Z. Wang, P. Xu, Q. Wang, J. He, *Angew. Chem., Int. Ed.* **2016**, *55*, 6919.
[24] F. Wang, T. A. Shifa, X. Zhan, Y. Huang, K. Liu, Z. Cheng, C. Jiang, J. He, *Nanoscale* **2015**, *7*, 19764.
[25] H. Zhou, F. Yu, Y. Liu, J. Sun, Z. Zhu, R. He, J. Bao, W. A. Goddard, S. Chen, Z. Ren, *Energy Environ. Sci.* **2017**, *10*, 1487.
[26] J. Yu, Q. He, G. Yang, W. Zhou, Z. Shao, M. Ni, *ACS Catal.* **2019**, *9*, 9973.
[27] S. Han, Q. Yun, S. Tu, L. Zhu, W. Cao, Q. Lu, *J. Mater. Chem. A* **2019**, *7*, 24691.
[28] Z. Zhang, P. Li, Q. Wang, Q. Feng, Y. Tao, J. Xu, C. Jiang, X. Lu, J. Fan, M. Gu, H. Li, H. Wang, *J. Mater. Chem. A* **2019**, *7*, 2780.
[29] Y. Zheng, Y. Jiao, Y. Zhu, L. H. Li, Y. Han, Y. Chen, M. Jaroniec, S.-Z. Qiao, *J. Am. Chem. Soc.* **2016**, *138*, 16174.
[30] J. Creus, J. De Tovar, N. Romero, J. García-Antón, K. Philippot, R. Bofill, X. Sala, *ChemSusChem* **2019**, *12*, 2493.
[31] Q. Lu, A.-L. Wang, H. Cheng, Y. Gong, Q. Yun, N. Yang, B. Li, B. Chen, Q. Zhang, Y. Zong, L. Gu, H. Zhang, *Small* **2018**, *14*, 1801090.
[32] K. Wang, Q. Chen, Y. Hu, W. Wei, S. Wang, Q. Shen, P. Qu, *Small* **2018**, *14*, 1802132.
[33] Y. Zhu, H. A. Tahini, Y. Wang, Q. Lin, Y. Liang, C. M. Doherty, Y. Liu, X. Li, J. Lu, S. C. Smith, C. Selomulya, X. Zhang, Z. Shao, H. Wang, *J. Mater. Chem. A* **2019**, *7*, 14222.
[34] J. Yu, Y. Guo, S. Miao, M. Ni, W. Zhou, Z. Shao, *ACS Appl. Mater. Interfaces* **2018**, *10*, 34098.
[35] X. Yang, Z. Zhao, X. Yu, L. Feng, *Chem. Commun.* **2019**, *55*, 1490.
[36] J. Wang, L. Han, B. Huang, Q. Shao, H. L. Xin, X. Huang, *Nat. Commun.* **2019**, *10*, 5692.
[37] H.-W. Liang, S. Liu, J.-Y. Gong, S.-B. Wang, L. Wang, S.-H. Yu, *Adv. Mater.* **2009**, *21*, 1850.
[38] J. K. Nørskov, T. Bligaard, A. Logadottir, J. R. Kitchin, J. G. Chen, S. Pandelov, U. Stimming, *J. Electrochem. Soc.* **2005**, *152*, J23.
[39] L. Zhang, Y. Jia, X. Yan, X. Yao, *Small* **2018**, *14*, 1800235.
[40] R. Wu, J. Zhang, Y. Shi, D. Liu, B. Zhang, *J. Am. Chem. Soc.* **2015**, *137*, 6983.
[41] X. Tian, P. Zhao, W. Sheng, *Adv. Mater.* **2019**, *31*, 1808066.
[42] Q. Wu, M. Luo, J. Han, W. Peng, Y. Zhao, D. Chen, M. Peng, J. Liu, F. M. F. de Groot, Y. Tan, *ACS Energy Lett.* **2020**, *5*, 192.
[43] L.-N. Zhang, Z.-L. Lang, Y.-H. Wang, H.-Q. Tan, H.-Y. Zang, Z.-H. Kang, Y.-G. Li, *Energy Environ. Sci.* **2019**, *12*, 2569.
[44] G. Chen, T. Wang, J. Zhang, P. Liu, H. Sun, X. Zhuang, M. Chen, X. Feng, *Adv. Mater.* **2018**, *30*, 1706279.
[45] J. Xu, T. Liu, J. Li, B. Li, Y. Liu, B. Zhang, D. Xiong, I. Amorim, W. Li, L. Liu, *Energy Environ. Sci.* **2018**, *11*, 1819.
[46] H. Li, X. Zhao, H. Liu, S. Chen, X. Yang, C. Lv, H. Zhang, X. She, D. Yang, *Small* **2018**, *14*, 1802824.
[47] J. Mahmood, F. Li, S.-M. Jung, M. S. Okyay, I. Ahmad, S.-J. Kim, N. Park, H. Y. Jeong, J.-B. Baek, *Nat. Nanotechnol.* **2017**, *12*, 441.
[48] Y. Liang, H. Wang, P. Diao, W. Chang, G. Hong, Y. Li, M. Gong, L. Xie, J. Zhou, J. Wang, T. Z. Regier, F. Wei, H. Dai, *J. Am. Chem. Soc.* **2012**, *134*, 15849.
[49] S. Chen, J. Duan, Y. Tang, B. Jin, S. Z. Qiao, *Nano Energy* **2015**, *11*, 11.
[50] A. A. Serov, M. Min, G. Chai, S. Han, S. Kang, C. Kwak, *J. Power Sources* **2008**, *175*, 175.
[51] A. Lewera, J. Inukai, W. P. Zhou, D. Cao, H. T. Duong, N. Alonso-Vante, A. Wieckowski, *Electrochim. Acta* **2007**, *52*, 5759.
[52] L. Jiao, F. Li, X. Li, R. Ren, J. Li, X. Zhou, J. Jin, R. Li, *Nanoscale* **2015**, *7*, 18441.
[53] Y. Ito, W. Cong, T. Fujita, Z. Tang, M. Chen, *Angew. Chem., Int. Ed.* **2015**, *54*, 2131.
[54] W. Zhou, J. Jia, J. Lu, L. Yang, D. Hou, G. Li, S. Chen, *Nano Energy* **2016**, *28*, 29.